UDC 623

M. UNAL, A. CALISKAN, Prof. Dr. A. S. TURK, P. O. BAKBAK

Turkey, Istanbul, Yildiz Technical University
E-mail: mehmetu@yildiz.edu.tr, acaliskan@yildiz.edu.tr, asturk@yildiz.edu.tr, pozkan@yildiz.edu.tr

SUBSURFACE AND THROUGH-WALL SAR IMAGING TECHNIQUES FOR GROUND PENETRATING RADAR

This paper presents some useful signal processing and synthetic aperture radar imaging techniques for ultra-wide band (UWB) ground penetrating radar. Novel UWB antenna structures are experimentally designed in this work. Raw and processed data collected in the course of experimental studies of subsurface sensing and through-wall imaging scenarios are demonstrated in B-scan and C-scan target images.

Keywords: ground penetrating radar, synthetic aperture radar, subsurface imaging, radar signal processing.

In the last decades, ground-penetrating radar **(GPR)** has become a leading non-destructive testing **(NDT)** technology for the detection, identification, and imaging of subsurface artifacts, abnormalities, and structures such as pipes, mines, gaps, water channels, oil wells, tunnels, and roads. It has a very broad range of applications, including geophysics, hydrogeology, archeology, mine detection, civil engineering, transportation, security and remote sensing [1—4]. GPR performance is associated with the electrical and magnetic properties of local soil and buried targets as well as with implementation of the GPR hardware and software. The frequency band of the GPR signal is the key factor for the detection performance. Higher frequencies are needed for better resolution, nevertheless lower frequency bands are preferred to detect something buried too deep due to the dramatically increased wave attenuation in the soil with increasing frequency. Thus, ultra-wide band **(UWB)** GPR systems that transmit short impulse signals are proposed primarily to benefit from both low and high frequencies [5].

The impulse durations can vary from a few nanoseconds to a hundred picoseconds corresponding to a broad spectrum from 100 MHz to 10 GHz. It can be extended up to 15 GHz for stepped-frequency GPR systems, which may use microwave tomography methods for high resolution imaging [6]. Therefore, the stepped-frequency **(SF)** technique offers some distinct signal processing benefits compared to the time-domain GPR systems, such as higher dynamic range and more effective control of the source frequency spectrum. Apart from increased resolution and increased depth of penetration, the signal spectrum received by SF-GPR provides the advantage of reading the real and phase parts, which can be made use of in analyzing subtle and complex inhomogeneities, particularly when carrying out tomographic inversion [7].

The subsurface target detection and imaging performances of the GPR depend significantly on the convenient design of UWB transmitter and receiver **(*T*/*R*)** antennas to radiate efficiently the GPR impulse signal into the buried or concealed target [8]. The antennas must have a flat, high-directivity gain, a narrow beam, and low side lobe and input reflection levels over the operational frequency band to reach the largest dynamic range, best focused illumination area, lowest level of *T*/*R* antenna coupling, reduced ringing, and uniformly shaped impulse radiation.

Synthetic aperture radar **(SAR)** is a well-known technique which uses signal processing to improve the resolution beyond the limitation of physical antenna aperture [9]. In SAR, forward motion of actual antenna is used to 'synthesize' a very long antenna. SAR allows the possibility of using longer wavelengths and still achieving good resolution with antenna structures of reasonable size. SAR is very useful over a wide range of applications, including sea and ice monitoring, mining, oil pollution monitoring, oceanography, snow monitoring, classifcation of earth terrain etc. [10].

In this study, a UWB SF-GPR system scenario is designed and realized by Rohde Schwarz ZVL-13 network analyzer. The network analyzer

This work was supported by grant 110E222 of TUBITAK (The Scientific and Technological Research Council of Turkey) research fund.

sweeps a wide signal band between 10 MHz and 15 GHz with 201 frequency steps. The continuous SF method is applied. The UWB transmitter and receiver antennas designed for this GPR system are the partial dielectric loaded transverse electromagnetic **(TEM)** fed ridged horn (PDTEM-RH) and Vivaldi shaped TEM horn (PDVA). Due to GPR data collecting process for *B*-scan plots requires simultaneous measurements, Basic macro codes are evaluated for data acquisition from the network analyzer to the PC. Moreover, by using the constructed SAR scenario, *B*-scan and *C*-scan images of subsurface and back wall objects with better resolution are exhibited in figures.

Antenna systems and measurements

The PDTEM horn, PDVA horn and array combinations have been introduced by A. S. Turk as efficient UWB impulse radiators operating from 150 MHz up to 10 GHz [11–14]. In this work, novel TEM and ridged horn antenna versions, which are operating in the frequency band of 400 MHz – 18 GHz, were designed with enhanced gain and VSWR performances. The measurement bandwidth is 10 MHz – 15 GHz. The antenna gain is sufficiently high and almost stable over the wide band. Instead of using dielectric aperture filling methods (i. e. hemispherical lenses) that increase the physical dimensions and weight of the antenna, the partial dielectric lens loading has been proposed for TEM horn and double-ridged horn antenna **(DRHA)** models to improve the gain performance and to eliminate radiation pattern deterioration without significant changes on the antenna sizes and weight.

It is shown that PDTEM and PDTEM-RH designs are highly suitable for multi-band GPR operations, due to advantages of up to 10 dB enhanced gain performances (in comparison with standard RH) over 1:40 bandwidth ratio.

Data acquisition and simultaneous test measurement

This study is devoted to data transfer from the network analyzer to the PC, signal processing techniques for transferred data, and post-processing by SAR algorithms. The network analyzer is set up for instantaneous measurement. However, *B*-scan GPR process requires simultaneous measurement. Thus, desired simultaneous measurements are collected by "for loop" written in Basic macro code. The measurement number is defined as 200. Also, the time interval between the simultaneous measurements is implemented by "sleep" command. This interval is set to 50 milliseconds.

An indoor test pool facility consisting of a wood box filled with dry soil has been constructed at our microwave research laboratory. The dimensions of the soil pool are 3.2×1.2×0.3 meters. The transmission coefficient S_{21} is measured by the network analyzer over the operational band. For *B*-scan and *C*-scan images data, S_{21} must be dependent on time. Therefore, the inverse Fourier transform of S_{21} is applied to obtain matrix

$$T = ifft(S_{21}). \quad (1)$$

The mathematical representation of "*ifft*" command is given as

$$T = \frac{1}{N}\sum_{n=0}^{N-1} S_{21} \exp\frac{-2\pi jkn}{N}, \quad (2)$$

where k represents the sampled points in the time domain, n represents the sampled points in the frequency domain, and N is the number of sampled points.

The background signal can be considered as a calibration or the reference signal for amelioration of the image of collected data. This signal consists of the direct pulse from transmitting and receiving antennas, ringing from the antennas, and clutter from other objects (not targets) that reflect the electromagnetic energy within the antenna beam width. The clutter can be minimized by using lower band radiator antennas. Nevertheless, this case will degrade the image resolution, which will cause hard-recognition of small buried objects. To reduce the clutter effect on *B*-scan plot, the reference signal is collected at the non-target position of the soil pool. If the transmission coefficient S_{21} dependent on time is symbolized by a, then background removed *A*-scan signal is calculated as

$$a_B(z) = \frac{1}{N}\sum_{i=1}^{N} a_i(z); \quad (3)$$

$$a_{BR}(z) = a(z) - a_B(z), \quad (4)$$

where a_B represents the non-target background signal; a_i is each *A*-scan data obtained from initial clear region and N is its number, and a_{BR} corresponds to background removed *A*-scan signal.

Then, the absolute of background removed T matrix is plotted by "surface" command and *B*-scan image is obtained:

$$B = |T|. \quad (5)$$

As shown in **Fig. 1**, the test measurement system of SF-GPR uses PDVA horn shown in **Fig. 2** as

Fig. 1. Measurement set up with network analyzer

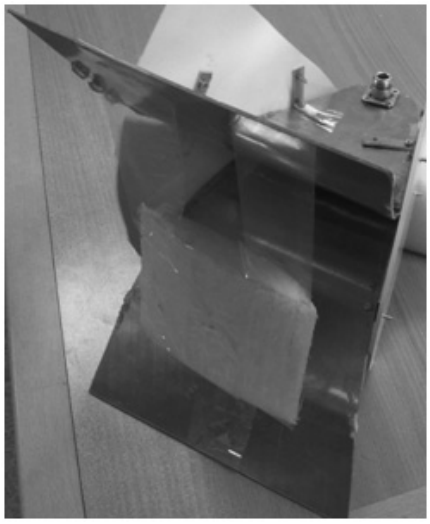

Fig. 2. Vivaldi shaped TEM horn design

Table 1

Test scenario of the buried objects

Parameters	Buried objects			
	Plastic pipe	Water pipe	Metal sheet	Glass (bottle)
Distance to reference point, cm	60	120	180	240
Depth, cm	3	3	3	3
Position	Vertical	Horizontal	Horizontal	Vertical

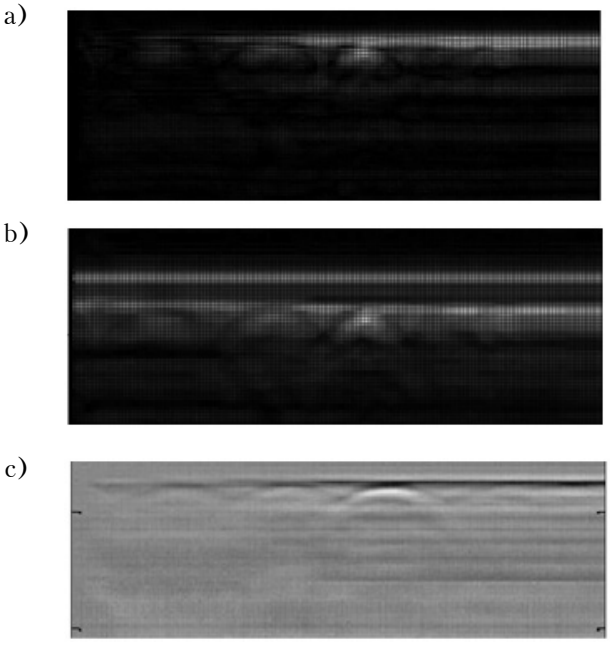

Fig. 3. *B*-scan measurement:
a — background removed; *b* — compressed sensing; *c* — data with impulse GPR

T/R antenna head. A typical metal plate separator is used for shielding between antennas so that coupling signal reduced. Buried objects scenario is given at **Table 1**. Measurement results of the *B*-scan data are plotted in **Fig. 3**, *a*, which can be seen successfully on the parabolas of the buried objects.

The reference signal is collected at the start point of the soil pool, although there can be slight differences between start and stop locations because of the heterogeneity of the soil. Fig. 3, *a* shows that four different types of objects can be detected clearly, and it is observed that metal plate reflects more signal as compared to other objects.

Another graphical representation of determining of position of the object is cumulative distribution, which represents the sum of vertical data changes on *B*-scan measurement data. As shown in **Fig. 4**, there are four peak points, which correspond to the correct cross-range positions of the buried objects. On the other hand, the compressed sensing technique is applied to collected data and four parabolas in Fig. 3, *b* are obtained more clearly than the image in Fig. 3, *a*. Obtained *B*-scan image by impulse GPR is given in Fig. 3, *c*.

For SAR test scenario, four objects (*U*-shaped metal strip, metal plate, water glass and dielectric plate) are buried as defined in **Table 2**. The operating principle scheme of fictive antenna array for SAR algorithm is shown in **Fig. 5**.

To obtain SAR beam of antenna at each scan point, a balance phase term is added to S_{21} pa-

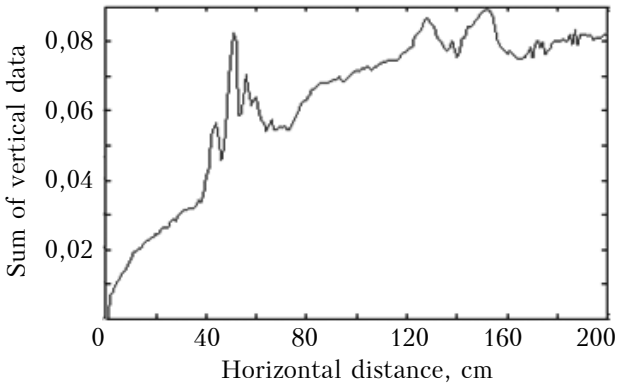

Fig. 4. Cumulative distribution of the buried objects

Table 2

Test scenario of SAR

Parameters	Buried objects			
	U-shaped metal strip	Metal plate	Water glass	Dielectric plate
Size, cm	20×30	10×10	6×20	10×12
Distance to the reference point, cm	80	150	184	220
Depth, cm	1	15	1	2
Position	Horizontal			

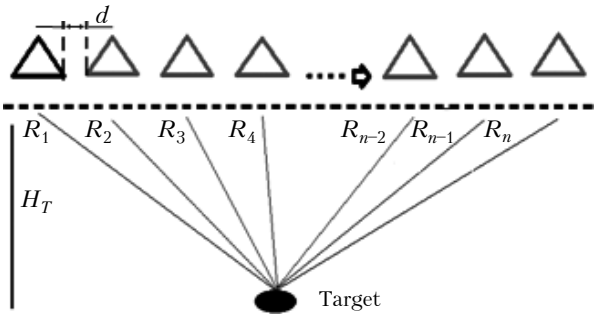

Fig. 5. Operating principle of fictive antenna array on SAR progress

rameter depending on the distance from location of n^{th} antenna to target point given as

$$R_n = \sqrt{H_T^2 + (nd)^2}, \quad (6)$$

where H_T^2 and d are vertical distance from location of reference antenna to target point and distance between antennas, respectively.

Difference between the distance from location of each antenna to the target point and the distance from location of reference antenna to the target point is given as

$$\Delta R_n = R_n - H_T. \quad (7)$$

Then, SAR effect to S parameter can be calculated as

$$S_{21SAR} = \sum_{n=1}^{N} S_{21} \exp(jk\Delta R_n), \quad (8)$$

where k and N are the wave number and the number of antennas, respectively.

Also, SAR length of this process is calculated as

$$L_{SAR} = N_d. \quad (9)$$

Three slices obtained from *C*-scan structure are given in **Fig. 6**. In this figure, the buried objects are clearly visible. Since the location of metal plate is deeper than the other objects and the soil

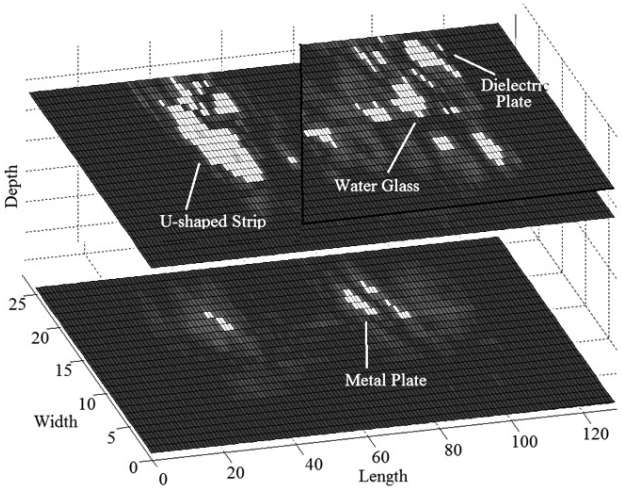

Fig. 6. SAR images for four buried objects (see in color on page 3 of the cover)

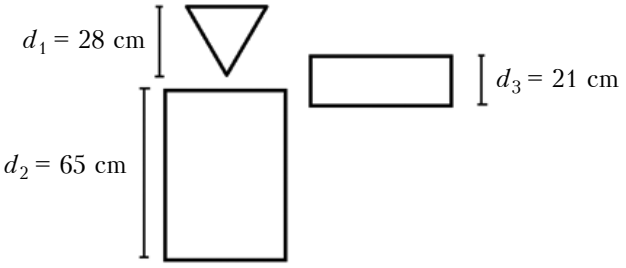

Fig. 7. Body model for TWI SAR operation

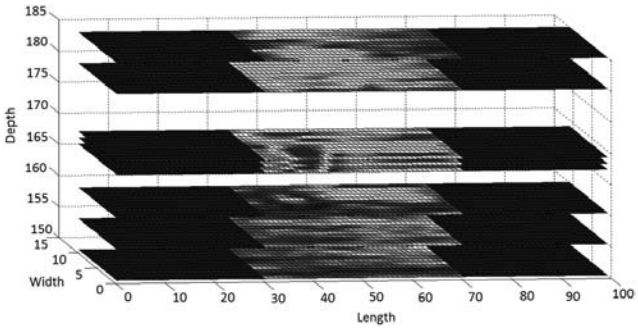

Fig. 8. C-scan slices of TWI SAR images (see in color on page 3 of the cover)

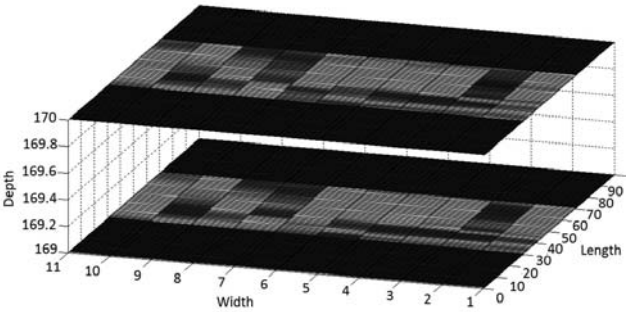

Fig. 9. Slices for the head and the trunk of the model (see in color on page 3 of the cover)

has high loss, the reflection from the metal plate is seen lower than *U*-shaped strip.

The other SAR application of our work is investigation of body model behind the brick wall. This target object model is shown in **Fig. 7**. The width of the wall is 50 cm. The distance from the wall to the target is 60 cm. The wall is almost homogeneous.

The *C*-scan slices of through-wall imaging SAR operation are given in **Fig. 8**. In this figure, it is seen that there is no object on near zone of the back wall, and the target body model behind the wall is clearly visible. The head and the trunk of body model can be seen in **Fig. 9**. It is seen that through-wall imaging SAR operation gives better resolution than the conventional GPR operation.

Conclusion

The target detection and signal processing performances of the ground penetrating radar are presented by using novel UWB partial dielectric loaded horn designs. The subsurface and through-wall imaging of the buried target objects are

demonstrated by using adaptive signal processing techniques in our GPR test scenario. It is shown that background removal, compressed sensing and SAR techniques provide enhanced resolution for imaging objects at different depths using novel antenna designs.

REFERENCES

1. Daniels D. J. Surface penetrating radar. *IEE Radar, sonar, navigation and avionics, series 6*. London, IEE, 1996.

2. Turk A. S., Hocaoglu A. K. Buried object detection. *In book: Encyclopedia of RF and microwave engineering,* Hoboken, NJ, Wiley-Interscience, 2005, vol. 1, pp. 541-559.

3. Borchert O., Aliman M., Glasmachers A. Directional borehole radar calibration. *Proc. of the 4th International Workshop on Advanced Ground Penetrating Radar (IWAGPR 2007)*, Naples (Italy), 2007, pp. 19-23.

4. MacDonald J., Lockwood J. R. *Alternatives for landmine detection*. Santa Monica, CA, RAND Science and Technology Policy, RAND Co., 2003.

5. Sahinkaya D. A., Turk A. S. UWB GPR for detection and identification of buried small objects. *Proc. SPIE*, 2004, vol. 5410, pp. 174-184.

6. Taylor D. *Ultra-wide band technology*. Boca Raton, FL, CRC Press, 2001.

7. Kong F. N., By T. L. Theory and performance of a GPR system which uses step frequency signals. *J. Appl. Geophys*, 1993, vol. 33, pp. 453-445.

8. Parrini F., Pieraccini M., Atzeni C. A high-speed continuous wave GPR. *In Proc. of the 10th International Conference on Ground Penetrating Radar*, Delft (The Netherlands), 2004, pp. 183-186.

9. Curlander J. C., McDounough R. N. *Synthetic aperture radar, systems and signal processing*. NewYork, John Wiley & Sons, 1991.

10. Chan Y. K., Koo V. C. An introduction to synthetic aperture radar (SAR). *Progress In Electromagnetics Research B*, 2008, vol. 2, pp. 27-60.

11. Turk A. S. Ultra-wideband Vivaldi antenna design for multi-sensor adaptive ground-penetrating impulse radar. *Microwave and Optical Technology Letters*, 2006, vol. 48, no 5, pp. 834-839.

12. Turk A. S., Sahinkaya D. A. Partial dielectric loaded TEM horn design for ultra-wideband ground penetrating impulse radar systems. *In book: Ultra-Wideband Short-Pulse Electromagnetics. Series 7. Chapter 34*. Berlin, Springer, 2007.

13. Turk A. S., Nazli H. Hyper-wide band TEM horn array design for multi band ground-penetrating impulse radar. *Microwave and Optical Technology Letters*, 2008, vol. 50, no 1, pp. 76-81.

14. Turk A. S., Keskin A. K. Partially dielectric-loaded ridged horn antenna design for ultrawide band gain and radiation performance enhancement. *IEEE Antennas and Wireless Propagation Letters*, 2012, vol. 11, pp. 921-924

Received 05.11 2013

M. Unal, A. Caliskan, A. S. Turk, P. O. Bakbak

Turkey, Istanbul, Yildiz Technical University

E-mail: mehmetu@yildiz.edu.tr, acaliskan@yildiz.edu.tr, asturk@yildiz.edu.tr, pozkan@yildiz.edu.tr

МЕТОДИ ОТРИМАННЯ РСА-ЗОБРАЖЕНЬ ЗАХОРОНЕНИХ ОБ'ЄКТІВ ДЛЯ ГЕОРАДАРА

У статті представлено методи обробки сигналу та отримання зображень за допомогою радіолокаційного синтезування апертури (РСА) для надширокосмугового (НШС) георадара. Запропоновано нові НШС-антенні структури. Результати експериментального дослідження методів підповерхневого зондування об'єктів, що знаходяться під землею і за стіною, представлені у вигляді зображень, отриманих B- та C-скануванням.

Ключові слова: георадар, радіолокатор з синтезованою апертурою, підповерхневе отримання зображень, обробка радіолокаційного сигналу.

M. Unal, A. Caliskan, A. S. Turk, P. O. Bakbak

Turkey, Istanbul, Yildiz Technical University

E-mail: mehmetu@yildiz.edu.tr, acaliskan@yildiz.edu.tr, asturk@yildiz.edu.tr, pozkan@yildiz.edu.tr

МЕТОДЫ ПОЛУЧЕНИЯ РСА-ИЗОБРАЖЕНИЙ ЗАХОРОНЕННЫХ ОБЪЕКТОВ ДЛЯ ГЕОРАДАРА

В статье представлены методы обработки сигнала и получения изображений при помощи радиолокационного синтезирования апертуры (РСА) для сверхширокополосного (СШП) георадара. Предложены новые СШП-антенные структуры. Результаты экспериментального исследования методов подповерхностного зондирования объектов, находящихся под землей и за стеной, представлены в виде изображений, полученных B- и C-сканированием.

Ключевые слова: георадар, радиолокатор с синтезированной апертурой; подповерхностное получение изображений, обработка радиолокационного сигнала.

К статье «Получение двухсторонних высоковольтных эпитаксиальных кремниевых $p-i-n$-структур методом ЖФЭ»

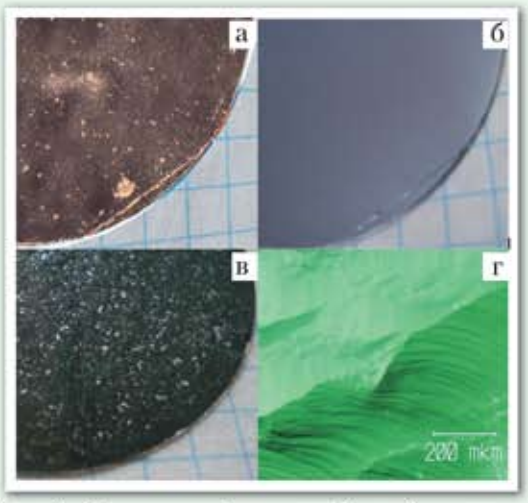

Рис. 2. Макроморфология (*а*–*в*) и микроморфология (*г*) поверхности *p*-Si-слоев, кристаллизованных в интервалах температуры 740–650°C из расплава Ga при различном содержании в нем алюминия (в ат. %):
а – 0,25; *б*, *г* – 0,76; *в* – 1,25

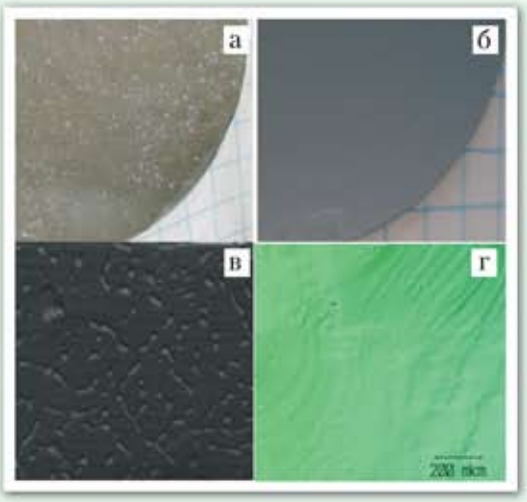

Рис. 4. Макроморфология (*а*–*в*) и микроморфология (*г*) поверхности *n*-Si-слоев, кристаллизованных в интервале температуры 850–750°C из расплава Sn, легированного сурьмой (8,5 ат. %), при различном содержании иттербия (в ат. %):
а – 0; *б*, *г* – 0,07; *в* – 0,18

К статье «Subsurface and through-wall SAR imaging techniques for ground penetrating radar»

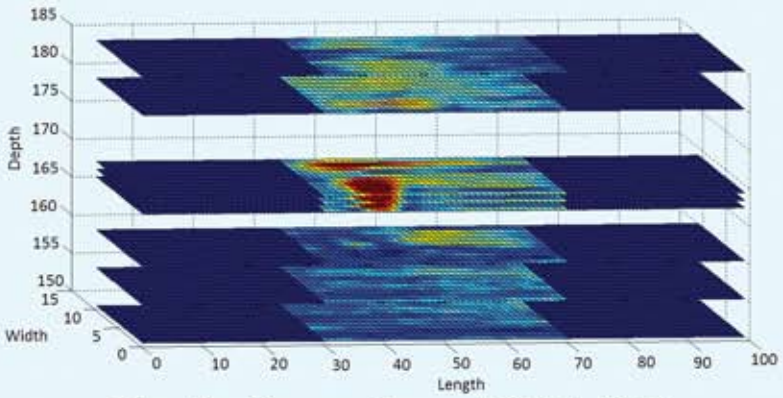

Fig. 8. C-scan slices of TWI SAR images

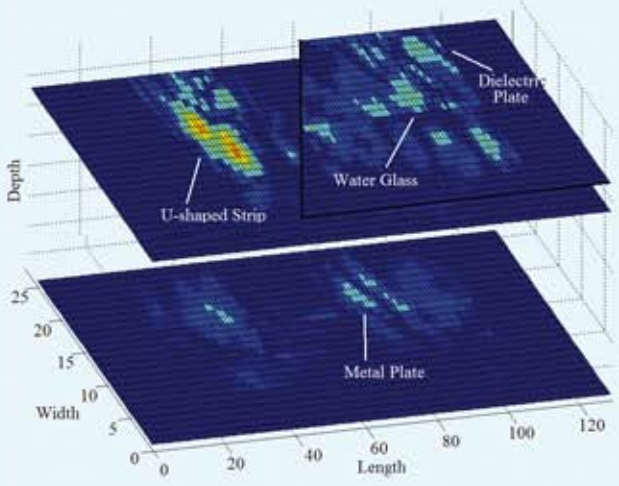

Fig. 6. SAR images for four buried objects

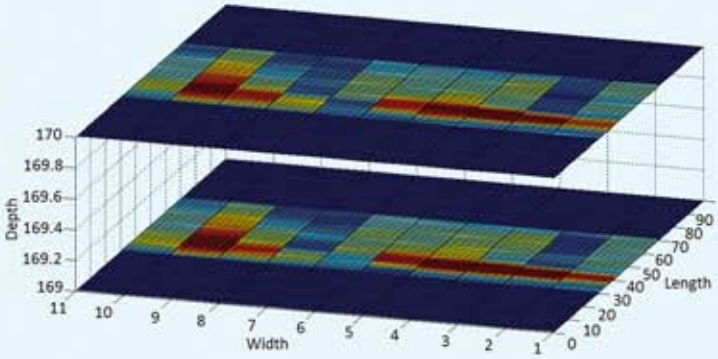

Fig. 9. Slices for the head and the trunk of model